

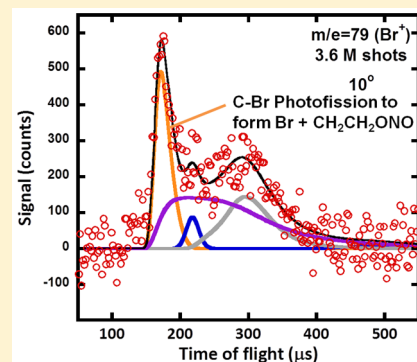
Competing C–Br and O–NO Photofission upon Excitation of BrCH₂CH₂ONO at 193 nm

Lei Wang, Preston G. Scrape, Trevor D. Roberts, Prakriti P. Joshi, and Laurie J. Butler*

The James Franck Institute and Department of Chemistry, The University of Chicago, Chicago, Illinois 60637 United States

S Supporting Information

ABSTRACT: This study characterizes two of the primary photodissociation channels of 2-bromoethyl nitrite, BrCH₂CH₂ONO, at 193 nm and the subsequent unimolecular dissociation channels of the nascent vibrationally excited BrCH₂CH₂O radicals produced from the O–NO bond photofission. We use a crossed laser-molecular beam scattering apparatus with electron bombardment detection. Upon photodissociation of BrCH₂CH₂ONO at 193 nm, the measured branching ratio between primary O–NO photofission and C–Br photofission is 3.9:1 (O–NO/C–Br). The measured O–NO photofission recoil kinetic energy distribution ($P(E_T)$) peaks near 30 kcal/mol and extends from 20 to 50 kcal/mol. We use the O–NO photofission $P(E_T)$ to characterize the internal energy distribution in the nascent ground-electronic-state BrCH₂CH₂O radicals. At 193 nm, all of the BrCH₂CH₂O radicals are formed with enough internal energy to unimolecularly dissociate to CH₂Br + H₂CO or to BrCH₂CHO + H. We also investigated the possibility of the BrCH₂CH₂O → CH₂CHO + HBr reaction arising from the vibrationally excited BrCH₂CH₂O radicals produced from O–NO primary photodissociation. Signal strengths at HBr⁺, however, demonstrate that the vinyloxy product does not have HBr as a cofragment, so the BrCH₂CH₂O → HBr + vinyloxy channel is negligible compared to the CH₂Br + H₂CO channel. We also report our computational prediction of the unimolecular dissociation channels of the vibrational excited CH₂CH₂ONO radical resulting from C–Br bond photofission. Our theoretical calculations on the ground-state CH₂CH₂ONO potential energy surface at the G4//B3LYP/6-311++G(3df,2p) level of theory give the energetics of the zero-point corrected minima and transition states. The lowest accessible barrier height for the unimolecular dissociation of CH₂CH₂ONO is a 12.7 kcal/mol barrier from the *cis*-ONO conformer, yielding NO₂ + ethene. Our measured internal energy distribution of the nascent CH₂CH₂ONO radicals together with this computational result suggests that the CH₂CH₂ONO radicals will dissociate to NO₂ + ethene, with a small possible branching to NO + oxirane.



1. INTRODUCTION

The formation of nitric oxide (NO) and its subsequent conversion to nitric acid is of significant environmental concern in atmospheric chemistry due to the latter's role in acid rain and its depletion effect on the ozone layer.¹ Alkyl nitrites (RONO, where R represents an alkyl moiety) have been shown to be a potential source of nitric oxide (NO) in the atmosphere. Interest in characterizing these important phenomena has led to previously reported studies on nitrous acid (HONO),^{2–5} methyl nitrite (CH₃ONO),^{6–10} and *tert*-butyl nitrite ((CH₃)₃CONO)^{11–14} photodissociation at a few different wavelengths. Several studies have focused on characterizing the photodissociation of alkyl nitrites. O–NO bond fission has been well studied near the 350 nm absorption band assigned to the S₀ → S₁ transition and near the 200 nm absorption band assigned to the S₀ → S₂ transition.¹⁵ The photodissociation of CH₃ONO, as a prototype, through the S₁ state represents an indirect process.¹⁶ The potential energy surface of the S₁ state has a shallow minimum above the ground-state equilibrium geometry, which has been proven experimentally and theoretically. However, excitation in the 200 nm absorption band reaches a potential energy surface of methyl nitrite, the S₂

state, that is strongly repulsive along the CH₃O...NO dissociation coordinate leading to a very rapid direct dissociation of the excited molecule.¹⁵

The photodissociation products from halogenated alkyl nitrites may be quite different from those of the well-studied alkyl nitrites described above. The carbon–halogen bond in the halogenated alkyl nitrite may be cleaved photolytically upon excitation at shorter wavelengths. Thus, this study investigates whether the carbon–halogen bond cleavage may compete with primary O–NO photofission upon excitation at 193 nm. In addition, the primary O–NO and C–X (X represents halogen) photofission channels may afford the opportunity to study the subsequent unimolecular dissociation of highly vibrationally excited bromoethoxy and nitrosooxy alkyl radicals. In our present work, 2-bromoethyl nitrite, BrCH₂CH₂ONO, was studied as prototype halogenated alkyl nitrite system.

Special Issue: Dynamics of Molecular Collisions XXV: Fifty Years of Chemical Reaction Dynamics

Received: April 30, 2015

Revised: June 22, 2015

In attempting to characterize the photodissociation of a halogenated alkyl nitrite through the S_1 state mentioned above, in our previous paper, we have reported a study of $\text{BrCH}_2\text{CH}_2\text{ONO}$ photodissociation at 351/355 nm.¹⁷ The only photodissociation channel of the precursor we detected upon photodissociation at 351 nm was O–NO bond fission. C–Br photofission and HBr photoelimination do not compete significantly with O–NO photofission at this excitation wavelength.

In this work, to further analyze the photodissociation of halogenated alkyl nitrites through the S_2 state, we focus on the primary photodissociation pathways of $\text{BrCH}_2\text{CH}_2\text{ONO}$ at 193 nm as the higher photon energy may induce C–Br bond fission in $\text{BrCH}_2\text{CH}_2\text{ONO}$ upon 193 nm excitation. This is possible because excitation at 193 nm excites the molecule both at the ONO chromophore and the C–Br chromophore, the latter corresponding to promoting the molecule to an excited state repulsive in the C–Br bond. Our present work measures this branching ratio between C–Br and O–NO primary channels. We also determine the internal energy distributions of $\text{BrCH}_2\text{CH}_2\text{O}$ radicals and $\text{CH}_2\text{CH}_2\text{ONO}$ radicals formed from the $\text{BrCH}_2\text{CH}_2\text{ONO}$ precursor photodissociation at 193 nm using a crossed laser-molecular beam scattering apparatus. We also calculate the energetics of the zero-point corrected minima and transition states on the ground-state $\text{CH}_2\text{CH}_2\text{ONO}$ potential energy surface at the G4//B3LYP/6-311++G(3df,2p) level of theory.

2. METHODS

2.1. Preparation of 2-Bromoethyl Nitrite ($\text{BrCH}_2\text{CH}_2\text{ONO}$). The experimental details relevant to this synthesis have been described previously.¹⁷ Briefly, a 100 mL aqueous solution of sodium nitrite (NaNO_2 , 4 M) was prepared in an ice bath. A mixture of 2-bromoethanol ($\text{BrCH}_2\text{CH}_2\text{OH}$, 0.4 mol), concentrated H_2SO_4 (0.2 mol), and deionized H_2O (7 mL) was added dropwise over 20 min with constant stirring. The organic layer of the final product, $\text{BrCH}_2\text{CH}_2\text{ONO}$, was collected and stored at -80°C to be used within 2 weeks.

2.2. Experimental Methods: Scattering Apparatus. We use a crossed laser-molecular beam scattering apparatus to measure the photofragment velocities resulting from O–NO fission and C–Br bond fission in the photodissociation of 2-bromoethyl nitrite, $\text{BrCH}_2\text{CH}_2\text{ONO}$, at 193 nm. The molecular beam is composed of $\text{BrCH}_2\text{CH}_2\text{ONO}$ seeded in helium gas to 600 Torr, using the equilibrium vapor pressure of $\text{BrCH}_2\text{CH}_2\text{ONO}$ in a -15°C bath. The continuous molecular beam is expanded through a nozzle with a 0.15 mm diameter orifice heated to 40°C . The molecular beam source can be rotated to different angles in the plane formed by the molecular beam and the detector axis. The parent beam is characterized at 0° by passing it through a chopper wheel operating at 200 Hz. To measure the velocities of the neutral fragments, we set the source angle to 10° . After supersonic expansion from the nozzle, the beam then passes through two skimmers en route to the main chamber, where it intersects the output of 193 nm unpolarized laser light focused to a $\sim 6\text{ mm}^2$ cross-sectional area. The 193 nm light is produced by the ArF transition of an unpolarized Lumonics PM-848 excimer laser and the energy at the crossing region with the molecular beam is 20 mJ/pulse. The laser light propagates along the axis perpendicular to the plane defined by the molecular beam and detector axis.

The neutral fragments scatter with velocities determined by the vector sum of the molecular beam's velocity and the recoil

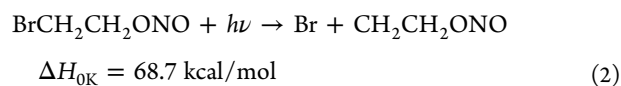
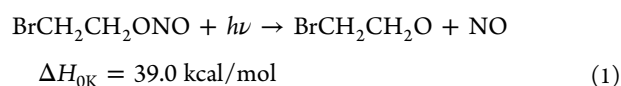
velocity imparted during the photodissociation. The products with a resultant velocity along the detector axis can be ionized by 200 eV electron bombardment ionization and then mass-to-charge selected by a quadrupole mass filter and detected using a Daly detector. The signal, proportional to the number of ions that strike the Daly detector as a function of time, is counted by a multichannel scaler and accumulated in $2\ \mu\text{s}$ channels. We can determine the neutral flight time by subtracting the calibrated ion flight time (4.5 multiplied by the square root of the detected ion mass) from the total flight time for each photofragment and subsequent products resulting from C–Br and O–NO fission. The data herein are plotted as a function of neutral flight time.

Beyond the data presented herein, we also looked for signal at $m/e = 74$ ($\text{CH}_2\text{CH}_2\text{ONO}^+$). At $m/e = 74$ ($\text{CH}_2\text{CH}_2\text{ONO}^+$), no signal appeared above the noise at the end of 5×10^5 laser shots. We also detected signal at $m/e = 42$, but present that data in a later paper, as it does not result from the $\text{BrCH}_2\text{CH}_2\text{O}$ radicals.

2.3. Computational Method. Our theoretical calculations on the ground-state $\text{CH}_2\text{CH}_2\text{ONO}$ potential energy surface at the G4//B3LYP/6-311++G(3df,2p) level of theory give the energetics of the zero-point corrected minima and transition states. Details are given in section 3.3. We also computationally characterize the equilibrium geometry of each possible conformer of the photolytic precursor, $\text{BrCH}_2\text{CH}_2\text{ONO}$, their relative energies and the C–Br bond energy to form $\text{Br}({}^2\text{P}_{3/2})$ and the lowest energy conformer (trans) of $\text{CH}_2\text{CH}_2\text{ONO}$. We use these geometries to model the angular momentum imparted to the recoiling $\text{CH}_2\text{CH}_2\text{ONO}$ radical.

3. RESULTS AND ANALYSIS

3.1. Overview of the Photodissociation Channels of $\text{BrCH}_2\text{CH}_2\text{ONO}$. Our theoretical and experimental results below provide evidence of two primary photodissociation channels, eqs 1 and 2: O–NO bond photofission and C–Br photofission. The calculated endoenergies are



“Primary dissociation” here means the first processes resulting from photodissociation at 193 nm, whereas secondary dissociation processes indicate the subsequent unimolecular dissociation of some of the vibrationally excited photoproducts. In later sections of this paper, we report experimental results on the secondary processes after the O–NO primary cleavage, as they are the processes relevant to our investigation of the $\text{BrCH}_2\text{CH}_2\text{O}$ radical intermediate. The secondary processes resulting from C–Br photodissociation and the unimolecular dissociation of $\text{CH}_2\text{CH}_2\text{ONO}$ are studied computationally in this paper but the experimental work using tunable VUV photoionization detection is ongoing.

3.2. O–NO Bond Fission Yielding $\text{BrCH}_2\text{CH}_2\text{O}$ and NO, and Subsequent Dissociation of Vibrationally Excited $\text{BrCH}_2\text{CH}_2\text{O}$. **3.2.1. O–NO Bond Primary Photodissociation.** The time-of-flight (TOF) spectrum taken at $m/e = 30$ (NO^+ , H_2CO^+) is shown in Figure 1. The high kinetic energy signal, peaking at arrival times around 110 μs in the spectrum, is the

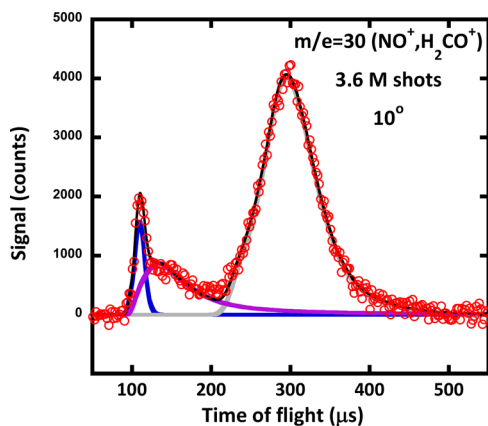


Figure 1. Time-of-flight spectrum of the signal at $m/e = 30$ (NO^+ , H_2CO^+). The data are shown in open circles and the overall fit is the sum of three contributions. The contribution to the signal from NO is a narrow component extending from 90 to 150 μs , assigned to $\text{O}-\text{NO}$ photofission eq 1 and fit as the blue line. The distribution of recoil kinetic energies, $P(E_T)$, for $\text{O}-\text{NO}$ bond photofission (193 nm excitation) derived from the forward convolution fitting of these data is shown in Figure 2; we assign the dominant fast component to $\text{O}-\text{NO}$ photofission. The contributions to this spectrum also include H_2CO products formed from secondary dissociation of those unstable vibrationally excited $\text{BrCH}_2\text{CH}_2\text{O}$ radicals formed with enough internal energy to surmount the barrier to $\text{CH}_2\text{Br} + \text{H}_2\text{CO}$; the fit is shown as a solid purple line. We use the $\text{O}-\text{NO}$ bond fission $P(E_T)$ in Figure 2 to determine the velocity of the radicals that dissociate and then iteratively adjust the distribution of relative kinetic energies $P(E_{T,2^\circ})$ shown in Figure 5 when the $\text{BrCH}_2\text{CH}_2\text{O}$ radicals dissociate to $\text{CH}_2\text{Br} + \text{H}_2\text{CO}$ to determine the additional velocity imparted to the CH_2Br product. The slower signal peaking near 300 μs fit as the gray solid line is attributed to the dissociation of molecular clusters ($(\text{BrCH}_2\text{CH}_2\text{ONO})_n$) in the beam. We use forward convolution fitting of this signal, where it is easily distinguishable and separable from other contributing signal sources, to derive a speed distribution associated with this cluster photodissociation.

NO photoproduct from primary $\text{O}-\text{NO}$ bond fission of the precursor, $\text{BrCH}_2\text{CH}_2\text{ONO}$. This channel forms vibrationally hot ground-state $\text{BrCH}_2\text{CH}_2\text{O}$ radicals + NO . We use forward convolution fitting of the fast peak near 110 μs to derive the $\text{O}-\text{NO}$ bond fission recoil kinetic energy distribution, $P(E_T)$, shown by the dashed blue line in Figure 2. It peaks near 30 kcal/mol in relative kinetic energy. In the time-of-flight (TOF) spectrum shown in Figure 1, the slower signal peaking near 300 μs (gray line) is attributed to the dissociation of molecular clusters ($(\text{BrCH}_2\text{CH}_2\text{ONO})_n$) in the beam. In this spectrum, signal from clusters is easily distinguishable and separable from other contributing signal sources, so we use the spectrum to determine the time-of-flight of signal from cluster photodissociation. The contributions to the signal at $m/e = 30$ in Figure 1 also include H_2CO products formed from secondary dissociation of the vibrationally excited $\text{BrCH}_2\text{CH}_2\text{O}$ radicals formed with enough internal energy to surmount the barrier to $\text{CH}_2\text{Br} + \text{H}_2\text{CO}$. This fit, shown as the purple line, is described in detail in section 3.2.4.

3.2.2. Internal Energy Distribution of Nascent $\text{BrCH}_2\text{CH}_2\text{O}$ Radicals. One main focus of our study is on the unimolecular dissociation of the momentum-matched $\text{BrCH}_2\text{CH}_2\text{O}$ radicals formed from photofission of the $\text{O}-\text{NO}$ bond; therefore, the distribution of internal energies in those nascent radicals is of interest. Using energy conservation, we can derive the internal

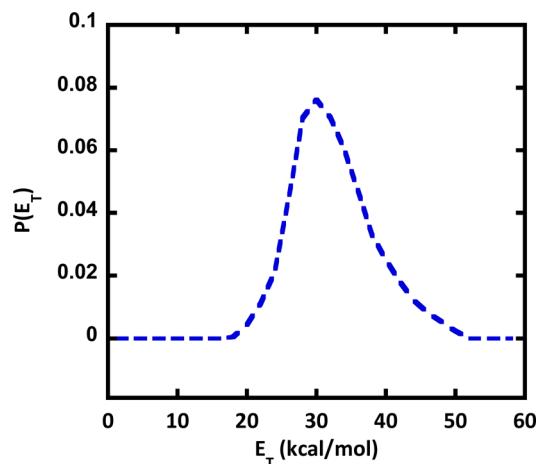


Figure 2. Total recoil kinetic energy distribution, $P(E_T)$, of the NO and $\text{BrCH}_2\text{CH}_2\text{O}$ resulting from $\text{O}-\text{NO}$ bond fission in the photodissociation of $\text{BrCH}_2\text{CH}_2\text{ONO}$ at 193 nm. The $P(E_T)$ (blue dashed line), peaking near 30 kcal/mol, is derived from the forward convolution fitting of the fast peak in the $m/e = 30$ (NO^+) signal in Figure 1.

energy distribution in the pair of nascent radicals (NO and $\text{BrCH}_2\text{CH}_2\text{O}$):

$$E_{\text{int}}(\text{BrCH}_2\text{CH}_2\text{O}) + E_{\text{int}}(\text{NO}) = h\nu + E_{\text{BrCH}_2\text{CH}_2\text{ONO}} - D_0(\text{O}-\text{NO}) - E_T \quad (3)$$

In eq 3, the 193 nm photon energy, $h\nu$, is 147.8 kcal/mol; $E_{\text{BrCH}_2\text{CH}_2\text{ONO}}$ is the internal energy of the $\text{BrCH}_2\text{CH}_2\text{ONO}$ precursor. Assuming the rotational energy of the precursor is effectively cooled in the supersonic expansion, the internal energy of precursor is estimated to be 2.84 kcal/mol in vibrational energy using a thermal distribution at the nozzle temperature of 40 °C. The dissociation energy of the $\text{O}-\text{NO}$ bond, $D_0(\text{O}-\text{NO})$, is 39.0 kcal/mol, calculated at the G4//B3LYP/6-311++G(3df,2p) level of theory. Subtracting our measured $\text{O}-\text{NO}$ bond fission recoil kinetic energy, E_T (with a distribution in Figure 2), the resulting internal energy distribution in the pair of products is shown in the top curve superimposed on a plot of the energetic barriers in Figure 3.

Even though we can determine the internal energy distribution of NO and $\text{BrCH}_2\text{CH}_2\text{O}$ directly by measuring the $P(E_T)$, one would prefer to know the internal energy distribution of the $\text{BrCH}_2\text{CH}_2\text{O}$ radicals alone because the NO carries away a significant amount of energy in vibration and rotation. To estimate the average amount of vibrational energy in the NO cofragment, we note that the UV absorption spectrum of $\text{BrCH}_2\text{CH}_2\text{ONO}$ has a similar shape and nearly the same maximum (peaking at 216 nm) as that of other alkyl nitrites, particularly CH_3ONO . Thus, we estimate the energy in vibration for our NO product using the vibrational distribution measured by Huber et al.¹⁸ for the dissociation of CH_3ONO in the S_2 band (the band accessed at 193 nm). The average vibrational energy they measure in the NO product is $\sim 3906 \text{ cm}^{-1}$. In addition, we also can use the prior results on CH_3ONO to estimate the rotational energy of the NO product. Even though the total recoil kinetic energy is different in CH_3ONO than in $\text{BrCH}_2\text{CH}_2\text{ONO}$, given the fact that the translational energy of the NO in the center-of-mass frame is very similar, close to 9000 cm^{-1} at the peak of the $P(E_T)$, we assume the energy partitioned to rotation of the NO would be

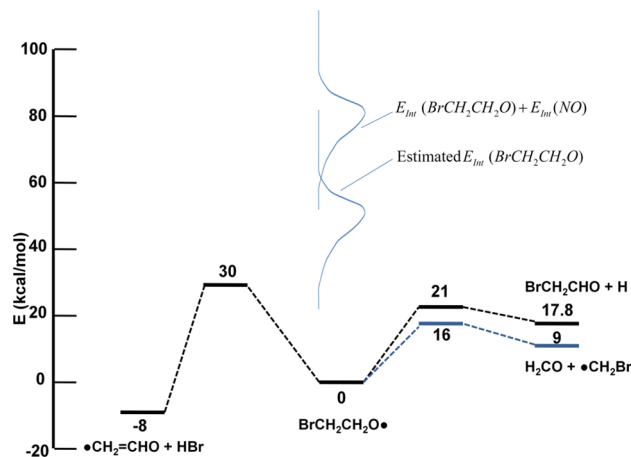


Figure 3. Internal energy distribution for nascent ground-state $\text{BrCH}_2\text{CH}_2\text{O}$ radicals formed in the photodissociation of $\text{BrCH}_2\text{CH}_2\text{ONO}$ at 193 nm. The upper curve, labeled $E_{\text{int}}(\text{BrCH}_2\text{CH}_2\text{O}) + E_{\text{int}}(\text{NO})$, is derived directly, using eq 3 in the text, from the major component of the O–NO photofission $P(E_T)$ peaking near $E_T = 30$ kcal/mol shown in Figure 2. The lower curve, which subtracts off the estimated average internal energy of 30 kcal/mol in the NO cofragment, peaks near an internal energy of 52 kcal/mol in the nascent $\text{BrCH}_2\text{CH}_2\text{O}$ radicals.

almost the same as for CH_3ONO photofission upon excitation in the analogous absorption feature. Therefore, we estimate the average rotational energy of NO to be about 6600 cm^{-1} on the basis of the rotational energies reported by Huber et al.¹⁸

To summarize, assuming the partitioning of vibrational and rotational energy to the NO cofragment is the same as alkyl nitrite excited in the analogous S_2 vibrational feature, we can roughly estimate the internal energy distribution of the $\text{BrCH}_2\text{CH}_2\text{O}$ radicals alone shown by the lower curve in Figure 3. The estimated internal energy distribution is superimposed on the calculated barriers to the dissociation of the $\text{BrCH}_2\text{CH}_2\text{O}$ radical. As only the average internal energy in the NO cofragment has been accounted for, the actual internal energy distribution would be somewhat broader than the lower curve shown in Figure 3. But it is clear that the internal energy distribution of the $\text{BrCH}_2\text{CH}_2\text{O}$ radicals allows all of the $\text{BrCH}_2\text{CH}_2\text{O}$ radicals to subsequently dissociate to $\text{CH}_2\text{Br} + \text{H}_2\text{CO}$ and other secondary dissociation channels.

3.2.3. $\text{CH}_2\text{Br} + \text{H}_2\text{CO}$ from the Dissociation of Vibrationally Excited $\text{BrCH}_2\text{CH}_2\text{O}$ Radicals. The $\text{BrCH}_2\text{CH}_2\text{O}$ radicals that are formed in conjunction with NO are formed with enough vibrational energy to surmount the dissociation barrier to $\text{CH}_2\text{Br} + \text{H}_2\text{CO}$ products. A fit of the signal observed at $m/e = 93$ (CH_2Br^+) is shown in Figure 4. The contributions to that spectrum include CH_2Br products formed from secondary dissociation of unstable vibrationally excited $\text{BrCH}_2\text{CH}_2\text{O}$ radicals, formed with enough internal energy to surmount the barrier to $\text{CH}_2\text{Br} + \text{H}_2\text{CO}$. That signal is fit as the purple line. The signal from clusters is fit as the gray line. To derive the distribution of relative kinetic energies $P(E_{T,2^\circ})$ when the $\text{BrCH}_2\text{CH}_2\text{O}$ radicals dissociate to $\text{CH}_2\text{Br} + \text{H}_2\text{CO}$ from our data, we use the entire O–NO bond fission $P(E_T)$ in Figure 2 to determine the velocity of the radicals that dissociate and then iteratively adjust the distribution of relative kinetic energies $P(E_{T,2^\circ})$ when the $\text{BrCH}_2\text{CH}_2\text{O}$ radicals dissociate to $\text{CH}_2\text{Br} + \text{H}_2\text{CO}$ to model the additional velocity imparted to the CH_2Br product. The fit shown as the purple line in Figure 4 was

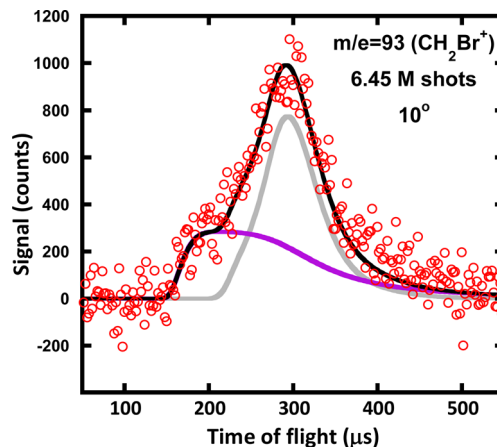


Figure 4. Time-of-flight spectrum of the signal at $m/e = 93$ (CH_2Br^+). The data are shown in open circles, and the overall fit is the sum of two contributions. The contributions shown as the solid purple line are assigned to CH_2Br products formed from secondary dissociation of unstable vibrationally excited $\text{BrCH}_2\text{CH}_2\text{O}$ radicals formed with enough internal energy to surmount the barrier to $\text{CH}_2\text{Br} + \text{H}_2\text{CO}$. We use the O–NO bond fission $P(E_T)$ in Figure 2 to determine the velocity of the radicals that dissociate and then iteratively adjust the distribution of relative kinetic energies $P(E_{T,2^\circ})$ shown in Figure 5 when the $\text{BrCH}_2\text{CH}_2\text{O}$ radicals dissociate to $\text{CH}_2\text{Br} + \text{H}_2\text{CO}$ to model the additional velocity imparted to the CH_2Br product with an isotropic $I(\theta)$ for the distribution of angles between the velocity vector of the dissociating radical and the additional velocity imparted to the radical as it dissociates. The contribution fit as the solid gray line is attributed to the photodissociation of clusters, and so is fit with the same speed distribution as the signal from clusters in Figure 1.

calculated from the primary $P(E_T)$ in Figure 2 and the secondary $P(E_T)$ in Figure 5 with an isotropic $I(\theta)$ for the distributions of angles between the velocity vector of the

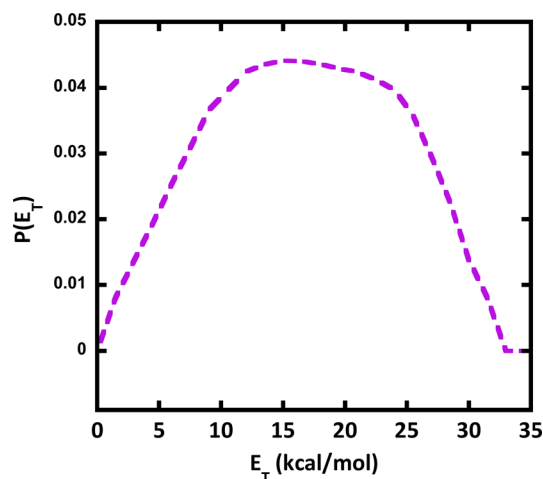


Figure 5. Recoil kinetic energy distribution $P(E_{T,2^\circ})$ for the dissociation of $\text{BrCH}_2\text{CH}_2\text{O}$ radicals to $\text{CH}_2\text{Br} + \text{H}_2\text{CO}$. The $P(E_{T,2^\circ})$ (purple dashed line) is derived from the forward convolution fitting of the broad purple peak in the $m/e = 30$ (NO^+) signal in Figure 1 to determine the velocity of the radicals that dissociate and then iteratively adjust the distribution of relative kinetic energies $P(E_{T,2^\circ})$ when the $\text{BrCH}_2\text{CH}_2\text{O}$ radicals dissociate to $\text{CH}_2\text{Br} + \text{H}_2\text{CO}$ to model the additional velocity imparted to fit the CH_2Br signal shown with a purple line in Figure 4. The distribution of angles, $I(\theta)$, is isotropic between the velocity vector of the dissociating radical and the additional velocity imparted to the radical as it dissociates.

dissociating radical and the additional velocity imparted to the radical as it dissociates.

To confirm the signal from the dissociation of the $\text{BrCH}_2\text{CH}_2\text{O}$ radicals to $\text{CH}_2\text{Br} + \text{H}_2\text{CO}$ products, we also identify signals from the momentum-matched formaldehyde (H_2CO) products formed when the $\text{BrCH}_2\text{CH}_2\text{O}$ radicals dissociate to $\text{CH}_2\text{Br} + \text{H}_2\text{CO}$ in the $m/e = 30$ spectrum shown in Figure 1. To fit the same contribution to the $m/e = 30$ (H_2CO^+) TOF spectrum in Figure 1 taken in our crossed laser-beam scattering apparatus, we also used the $P(E_T)$ shown in Figure 2 and the secondary kinetic energy distribution $P(E_{T,2^\circ})$ shown in Figure 5 predicted from fitting $m/e = 93$ (CH_2Br^+) TOF spectrum.

We also note that formaldehyde (H_2CO) can be dissociatively ionized to form CHO^+ upon high-energy (200 eV) electron bombardment ionization; this can confirm the presence of the $\text{CH}_2\text{Br} + \text{H}_2\text{CO}$ channel. In the signal at $m/e = 29$ (CHO^+) shown in Figure 6, the major contributions

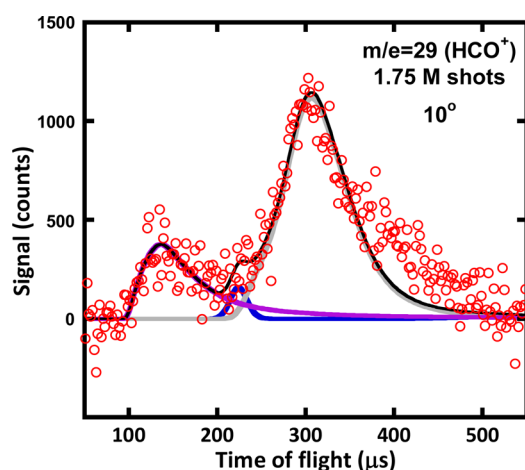


Figure 6. Time-of-flight (TOF) spectrum taken at $m/e = 29$ (CHO^+). The three contributions to the signal include (1) dissociative ionization of CH_2O resulting from secondary dissociation of the unstable vibrationally excited $\text{BrCH}_2\text{CH}_2\text{O}$ radicals (solid purple line), (2) dissociative ionization of BrCH_2CHO resulting from secondary dissociation of the unstable vibrationally excited $\text{BrCH}_2\text{CH}_2\text{O}$ radicals (solid blue line), and (3) signal from the photodissociation of clusters (solid gray line). We use the O–NO bond fission $P(E_T)$ in Figure 2 to determine the velocity of the $\text{BrCH}_2\text{CH}_2\text{O}$ radicals that dissociate (assuming they are formed throughout the entire recoil energy distribution) and the distribution of relative kinetic energies $P(E_{T,2^\circ})$ shown in Figure 5 when the $\text{BrCH}_2\text{CH}_2\text{O}$ radicals dissociate to $\text{CH}_2\text{Br} + \text{H}_2\text{CO}$ to model the additional velocity imparted to the CH_2O product.

to that spectrum include H_2CO products formed from secondary dissociation of those unstable vibrationally excited $\text{BrCH}_2\text{CH}_2\text{O}$ radicals, fit as the purple line, and signal from clusters, fit as the gray line. For the first contribution, we used the blue line $P(E_T)$ shown in Figure 2 and the secondary kinetic energy distribution $P(E_{T,2^\circ})$ shown in Figure 5 predicted from fitting the $m/e = 93$ (CH_2Br^+) TOF spectrum. For completeness, Figure 6 also shows, as the blue line, a possible signal from dissociative ionization of the BrCH_2CHO fit (see next section).

3.2.4. $\text{H} + \text{BrCH}_2\text{CHO}$ from the Dissociation of Vibrationally Excited $\text{BrCH}_2\text{CH}_2\text{O}$ Radicals. The internal energy distribution of the $\text{BrCH}_2\text{CH}_2\text{O}$ radicals shown in Figure 3 is high enough to allow $\text{BrCH}_2\text{CH}_2\text{O}$ radicals to dissociate to $\text{H} +$

BrCH_2CHO (in addition to the major $\text{CH}_2\text{Br} + \text{H}_2\text{CO}$ channel); thus, signal from this channel is expected. Because of the large mass ratio between BrCH_2CHO and H , the velocity of the resulting BrCH_2CHO molecule is approximately the same as the velocity of the $\text{BrCH}_2\text{CH}_2\text{O}$ radical that underwent C–H fission. Therefore, the speed of the BrCH_2CHO fragment in this secondary dissociation should be well predicted by only the primary $P(E_T)$ shown in Figure 2. However, BrCH_2CHO does not give signal for the parent ion due to the high-energy (200 eV) electron bombardment ionization but instead was dissociatively ionized to give small signals fit as the solid blue line for the CHO^+ ion (Figure 6), HBr^+ ion (Figure 7), and Br^+

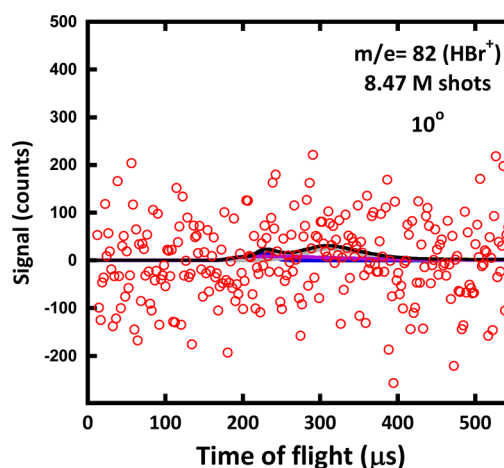


Figure 7. Time-of-flight spectrum of the signal at $m/e = 82$ (HBr^+). The data are shown as open circles. Virtually no signal is apparent, but for completeness we show the flight time of three possible contributions to the spectrum: dissociative ionization of BrCH_2CHO to HBr^+ (solid blue line) and dissociative ionization of CH_2Br radicals from secondary dissociation from $\text{BrCH}_2\text{CH}_2\text{O}$ radicals to $\text{CH}_2\text{Br} + \text{H}_2\text{CO}$ (solid purple line) and clusters (solid gray line).

daughter ion (Figure 8). Dissociative ionization at $m/e = 42$ is reported in a publication in preparation, as some of the signal in the spectrum is from a channel not reported here.

3.2.5. Absence of the $\text{HBr} + \text{Vinoxy}$ Channel from the Dissociation of $\text{BrCH}_2\text{CH}_2\text{O}$ Radicals. On the basis of the theoretical prediction of the barrier energies on the $\text{BrCH}_2\text{CH}_2\text{O}$ potential energy surface, one would estimate the probability of secondary dissociation to $\text{HBr} + \text{vinoxy}$ from vibrationally excited $\text{BrCH}_2\text{CH}_2\text{O}$ radicals to be small. The calculated barrier of 39 kcal/mol is much larger than the 16 kcal/mol barrier en route to the $\text{H}_2\text{CO} + \text{CH}_2\text{Br}$ product channel. The signal at $m/e = 82$ (HBr^+) shown in Figure 7 is barely observable after 8.47 million shots despite the fact that the electron bombardment cross section of HBr is relatively large. For completeness, we show three possible small contributions to fit the tiny signal: dissociative ionization of BrCH_2CHO formed from the minor unimolecular dissociation channel of the $\text{BrCH}_2\text{CH}_2\text{O}$ radical to $\text{BrCH}_2\text{CHO} + \text{H}$ fit as the solid blue line; dissociative ionization of CH_2Br formed from the major unimolecular dissociation channel of the $\text{BrCH}_2\text{CH}_2\text{O}$ radical to $\text{CH}_2\text{Br} + \text{H}_2\text{CO}$ fit as the solid purple line; dissociation of clusters as the solid gray line. There is no apparent contribution from the unimolecular dissociation of $\text{BrCH}_2\text{CH}_2\text{O}$ to $\text{HBr} + \text{vinoxy}$. Therefore, we conclude the $\text{HBr} + \text{vinoxy}$ secondary channel is negligibly small.

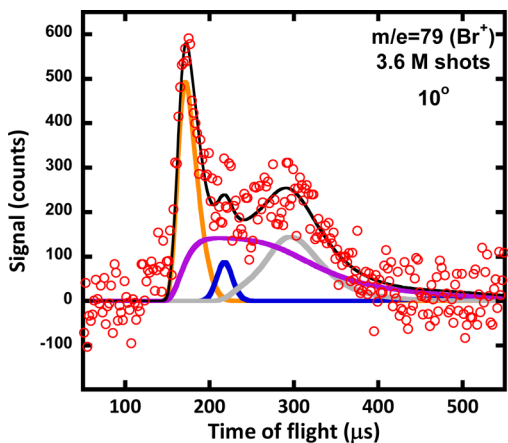


Figure 8. Time-of-flight (TOF) spectrum taken at $m/e = 79$ (Br^+). Four contributions to the spectrum include Br products formed from primary C–Br bond fission from the precursor (orange line), Br^+ from the dissociative ionization of CH_2Br resulting from secondary dissociation of the unstable vibrationally excited $\text{BrCH}_2\text{CH}_2\text{O}$ radicals (solid purple line), signal from the dissociative ionization of bromoacetaldehyde BrCH_2CHO from secondary dissociation of the $\text{BrCH}_2\text{CH}_2\text{O}$ radicals (solid blue line), and signal from cluster photodissociation (solid gray line). The high kinetic energy signal fit by the orange line, peaking at an arrival time near $180 \mu\text{s}$ in the spectrum, is the Br photoproduct from primary C–Br bond fission of the precursor. For the second contribution, we use the O–NO bond fission $P(E_T)$ in Figure 2 to determine the velocity of the radicals that dissociate and the distribution of relative kinetic energies $P(E_{T,2^\circ})$ shown in Figure 6 when the $\text{BrCH}_2\text{CH}_2\text{O}$ radicals dissociate to $\text{CH}_2\text{Br} + \text{H}_2\text{CO}$ to model the additional velocity imparted to the CH_2Br product. The contribution fit as the solid blue line from the dissociative ionization of BrCH_2CHO is derived from the $P(E_T)$ in Figure 2.

Moreover, we note that HBr would be also dissociatively ionized to Br^+ upon 200 eV electron bombardment ionization. In the $m/e = 79$ (Br^+) TOF spectrum shown in Figure 8, there is no apparent contribution from dissociatively ionized HBr after secondary dissociation from $\text{BrCH}_2\text{CH}_2\text{O}$ nascent radicals to $\text{HBr} + \text{vinoxy}$ photoproducts.

3.3. C–Br Photodissociation Yielding $\text{CH}_2\text{CH}_2\text{ONO} + \text{Br}$ and Theoretical Prediction of Nascent $\text{CH}_2\text{CH}_2\text{ONO}$ Unimolecular Decomposition. **3.3.1. Primary Photodissociation of $\text{BrCH}_2\text{CH}_2\text{ONO}$ to $\text{CH}_2\text{CH}_2\text{ONO} + \text{Br}$.** Previous studies of $\text{BrCH}_2\text{CH}_2\text{ONO}$ at 351 nm¹⁷ focused heavily on the unimolecular decomposition pathways of the momentum matched $\text{BrCH}_2\text{CH}_2\text{O}$ radical formed from the photofission of the O–NO bond. This study of $\text{BrCH}_2\text{CH}_2\text{ONO}$ at 193 nm allows us to study a different photofission-generated radical, the $\text{CH}_2\text{CH}_2\text{ONO}$ radical. This is possible because excitation at 193 nm excites the molecule both at the O–NO chromophore and the C–Br chromophore, the latter corresponding to promoting the molecule to an excited state repulsive in the C–Br bond.

The time-of-flight (TOF) spectrum taken at $m/e = 79$ (Br^+) is shown in Figure 8. Four contributions to that spectrum include Br products (orange line) formed from primary C–Br bond fission of the precursor, dissociative ionization from CH_2Br (purple line) resulting from secondary dissociation of the unstable vibrationally excited $\text{BrCH}_2\text{CH}_2\text{O}$ radicals and dissociative ionization of BrCH_2CHO (blue line) from the $\text{BrCH}_2\text{CHO} + \text{H}$ secondary channel and clusters (gray line). The high kinetic energy signal shown as the orange line,

peaking at arrival times around $180 \mu\text{s}$ in the spectrum, is the Br photoproduct from primary C–Br bond fission of the precursor. We use forward convolution fitting of the fast peak near $180 \mu\text{s}$ to derive the C–Br bond fission recoil kinetic energy distribution $P(E_T)$, shown as the dashed orange line in Figure 9. It peaks near 28 kcal/mol in relative kinetic energy.

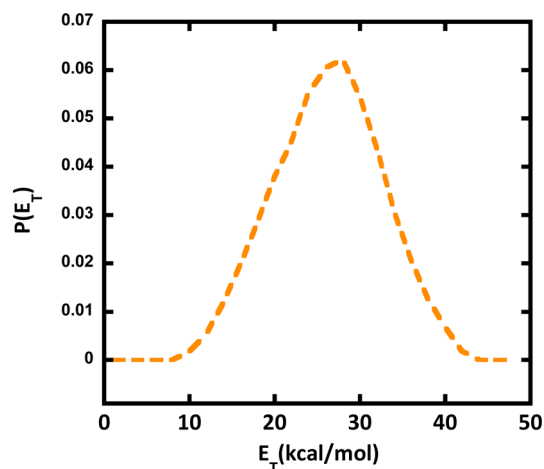


Figure 9. Total recoil kinetic energy distribution, $P(E_T)$, of the Br and $\text{CH}_2\text{CH}_2\text{ONO}$ resulting from C–Br bond fission in the photodissociation of $\text{BrCH}_2\text{CH}_2\text{ONO}$ at 193 nm. The $P(E_T)$ (orange dashed line), peaking near 28 kcal/mol, is derived from the forward convolution fitting of the fast peak in the $m/e = 79$ (Br^+) signal in Figure 8.

To fit the signal from dissociative ionization of CH_2Br , we used the $P(E_T)$ shown in Figure 2 and the secondary kinetic energy distribution $P(E_{T,2^\circ})$ predicted from fitting the $m/e = 93$ (CH_2Br^+) TOF spectrum shown in Figure 5 in conjunction with an isotropic $I(\theta)$ for the distributions of angles between the velocity vector of the dissociating radical and the additional velocity imparted to the radical as it dissociates. The fit to the signal from dissociative ionization of stable BrCH_2CHO (blue line) was calculated using the previously determined $P(E_T)$ in Figure 2, as described in section 3.2.4.

3.3.2. Theoretical Prediction of Nascent $\text{CH}_2\text{CH}_2\text{ONO}$ Unimolecular Decomposition. We are interested in the internal energy distribution of nascent $\text{CH}_2\text{CH}_2\text{ONO}$ (2-nitrosooxy ethyl) radicals and their relevant unimolecular decomposition pathways, so we used electronic structure theory to predict the barriers and minima along several possible ground-state dissociation pathways of the radical. Our theoretical calculations on the ground-state $\text{CH}_2\text{CH}_2\text{ONO}$ potential energy surface at the G4//B3LYP/6-311++G(3df,2p) level of theory give the energetics of the zero-point corrected minima and transition states shown in Figure 10. Depending on the geometric conformations of the initial photolytic precursor, $\text{BrCH}_2\text{CH}_2\text{ONO}$, the primary C–Br photodissociation event may yield vibrationally and rotationally excited $\text{CH}_2\text{CH}_2\text{ONO}$ radicals in one of two conformers: a trans or a cis conformer in the C–ONO moiety. The channel with the lowest barrier is actually an isomerization channel from the trans- $\text{CH}_2\text{CH}_2\text{ONO}$ radical conformer to the cis $\text{CH}_2\text{CH}_2\text{ONO}$ radical conformer by surmounting a barrier of 11.4 kcal/mol. Other barrier heights of interest concern unimolecular dissociation product channels and isomerization channels leading toward dissociation products. Should the $\text{CH}_2\text{CH}_2\text{ONO}$ radicals have enough internal energy, a 12.7 kcal/mol barrier may be surmounted

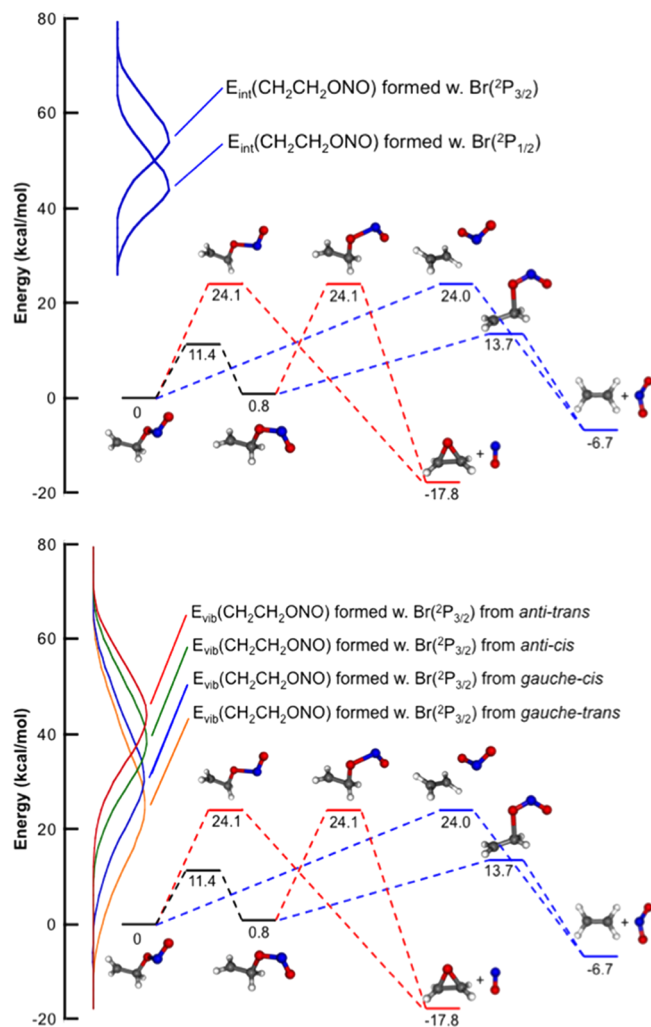


Figure 10. Internal energy distribution (upper frame) and vibrational energy distribution (lower frame) for nascent ground-state $\text{CH}_2\text{CH}_2\text{ONO}$ radicals formed in the photodissociation of $\text{BrCH}_2\text{CH}_2\text{ONO}$ at 193 nm. These distributions are superimposed on the critical points on the potential energy surface calculated at the G4//B3LYP/6-311++G(3df,2p) level of theory.

along the intrinsic reaction coordinate (IRC) from the cis $\text{CH}_2\text{CH}_2\text{ONO}$ radical to the CH_2CH_2 (ethene) + NO_2 product asymptote. Another pathway from the cis $\text{CH}_2\text{CH}_2\text{ONO}$ conformer is the competitive 23.3 kcal/mol barrier along the IRC toward the three-member ring $\text{CH}_2\text{CH}_2\text{O}$ (ethylene oxide or oxirane) + NO asymptote. These two channels, NO_2 + CH_2CH_2 and NO + $\text{CH}_2\text{CH}_2\text{O}$, are also available to the trans radical conformer, except with a 24.0 and 24.1 kcal/mol barrier to dissociation, respectively. Another relevant product channel beginning from the *trans*- $\text{CH}_2\text{CH}_2\text{ONO}$ radical involves an isomerization to the $\text{CH}_2\text{CH}_2\text{NO}_2$ radical through a four-membered ring intermediate en route to NO_2 + ethene. Along this pathway, not shown in Figure 10, first a 14.2 kcal/mol barrier is surmounted to yield a relatively stable ground-state four-membered ring at -1.3 kcal/mol. This intermediate can further isomerize to $\text{CH}_2\text{CH}_2\text{NO}_2$ by surmounting a 30.0 kcal/mol barrier, after which the $\text{CH}_2\text{CH}_2\text{NO}_2$ radical will certainly dissociate toward the NO_2 + CH_2CH_2 product asymptote after surmounting a 9.2 kcal/mol barrier.

3.3.3. Internal Energy Distribution of Nascent $\text{CH}_2\text{CH}_2\text{ONO}$ Radicals. Estimating the internal energy dis-

tribution of the $\text{CH}_2\text{CH}_2\text{ONO}$ radicals required measuring the relative kinetic energy of the recoiling Br and $\text{CH}_2\text{CH}_2\text{ONO}$ radicals and the internal energy of the Br radical cofragment. In Figure 10, we show our estimate of the internal energy distribution of the nascent ground-electronic-state $\text{CH}_2\text{CH}_2\text{ONO}$ radicals superimposed on a plot of the energetic barriers the radical must surmount to undergo subsequent isomerization and dissociation. We derived the C–Br fission E_T through a forward convolution fit to the $m/e = 79$ ($^{79}\text{Br}^+$) time-of-flight spectrum and momentum matching to the $\text{CH}_2\text{CH}_2\text{ONO}$ radical to generate said C–Br bond fission recoil kinetic energy, E_T , and apply this relative translational energy distribution, $P(E_T)$, directly to our conservation of energy equation:

$$E_{\text{int}}(\text{CH}_2\text{CH}_2\text{ONO}) + E_{\text{int}}(\text{Br}) = h\nu + E_{\text{BrCH}_2\text{CH}_2\text{ONO}} - D_0(\text{C} - \text{Br}) - E_T \quad (4)$$

In eq 4, the 193 nm photon energy, $h\nu$, is 147.8 kcal/mol; the dissociation energy of the C–Br bond, the value of $D_0(\text{C} - \text{Br})$ for each conformer, is shown in Table 1, calculated at the G4//B3LYP/6-311++G(3df,2p) level of theory. $E_{\text{BrCH}_2\text{CH}_2\text{ONO}}$ is the internal energy of the $\text{BrCH}_2\text{CH}_2\text{ONO}$ photolytic precursor—we assume the rotational energy of the precursor is effectively cooled in the supersonic expansion and the vibrational energy is estimated by a thermal distribution, with an average 2.84 kcal/mol, at the nozzle temperature of 40 °C. The final parameter of eq 4, $E_{\text{int}}(\text{Br})$, is the internal energy of recoiling bromine atoms, as they may be formed in either the ground $\text{Br}(^2\text{P}_{3/2})$ or the excited $\text{Br}(^2\text{P}_{1/2})$ spin–orbit state, which differ in energy by 10.5 kcal/mol. Bromine atoms in the $\text{Br}(^2\text{P}_{1/2})$ spin–orbit state are 10.5 kcal/mol higher in energy than bromine atoms in the $\text{Br}(^2\text{P}_{3/2})$ spin–orbit state.

The upper frame in Figure 10 shows our estimate of the internal energy distributions of $\text{CH}_2\text{CH}_2\text{ONO}$ radicals superimposed upon the ground-state potential energy surface with zero-point corrected minima and transition states along pathways toward isomerization and unimolecular dissociation. The two internal energy distributions shown reflect the fact that we have not determined the spin–orbit state of the Br atom coproduct. If the Br atom is formed in the ground spin–orbit state $\text{Br}(^2\text{P}_{3/2})$, then the $\text{CH}_2\text{CH}_2\text{ONO}$ radicals would have the higher internal energy distribution shown in Figure 10. This internal energy of $\text{CH}_2\text{CH}_2\text{ONO}$ is partitioned between rotational and vibrational energy, so some of the radicals with a total internal energy above the dissociation barrier may still be stable to subsequent dissociation due to a relatively larger proportion of rotational energy as a result of conservation of angular momentum.

3.3.4. Vibrational Energy Distribution of Nascent $\text{CH}_2\text{CH}_2\text{ONO}$ Radicals. The C–Br photofission partitions a large amount of energy into rotation of the $\text{CH}_2\text{CH}_2\text{ONO}$ radicals; less energy is then partitioned to vibration of the radicals. Not only does this result in some $\text{CH}_2\text{CH}_2\text{ONO}$ radicals that are stable to the secondary dissociation, but the product branching from the unstable ones is altered by the amount of energy constrained to be rotational energy due to conservation of angular momentum. To estimate this angular momentum, we first use the method discussed in McKown et al.¹⁹ to calculate the distribution, shown in Figure 11, of the magnitude of the angular momentum vectors, $P(J)$, imparted to the nascent $\text{CH}_2\text{CH}_2\text{ONO}$ radicals following the photo-

Table 1. 2-Bromoethyl Nitrite

conformer	skeleton structure	relative energy (kcal/mol) ^a	D_0 (C-Br) (kcal/mol) ^b
anti-trans		0.00	68.77
gauche-trans		0.19	68.57
anti-cis		0.70	68.07
gauche-cis		1.34	67.43

^aThe relative energy of each conformer is with respect to the anti-trans conformer. ^bThe bond energy is calculated to form $\text{Br}(^2\text{P}_{3/2})$ and the lowest energy conformer (trans) of $\text{CH}_2\text{CH}_2\text{ONO}$.

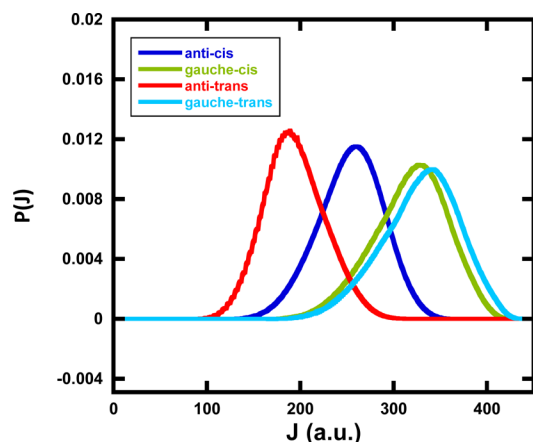


Figure 11. Angular momentum distribution, $P(J)$ distribution for *trans*- $\text{CH}_2\text{CH}_2\text{ONO}$ radicals produced from each of the four conformers of $\text{BrCH}_2\text{CH}_2\text{ONO}$. The distributions peak at 190, 260, 320, and 330 au, respectively, indicating that a large rotational energy is imparted to the nascent radicals. The distributions are convolved over all possible internal energies of the parent molecule, and over all possible translational energies from the experimentally determined $P(E_T)$ distribution.

dissociation of each of the four precursor conformers. The distributions peak at 190, 260, 320, and 330 au for radicals from each conformer, respectively. The distributions are convolved over all possible internal energies of the parent molecule and over all possible translational energies from the experimentally determined $P(E_T)$ distribution. The supplementary document shows in Figure S1 more detail, slices of the J distribution along selected internal energies of the radicals produced from each of the four conformers. The lower frame in Figure 10 shows the resulting estimate of the vibrational energy distributions of *trans*- $\text{CH}_2\text{CH}_2\text{ONO}$ radicals formed from the four precursor

conformers superimposed upon the ground-state potential energy surface of $\text{CH}_2\text{CH}_2\text{ONO}$ radicals. Because the energy difference between ground spin-orbit state $\text{Br}(^2\text{P}_{3/2})$ and excited spin-orbit state $\text{Br}(^2\text{P}_{1/2})$ is 10.5 kcal/mol, we only show the four vibrational energy distributions for radicals formed in conjunction with ground spin-orbit state $\text{Br}(^2\text{P}_{3/2})$. If the Br atom is formed in the excited spin-orbit state $\text{Br}(^2\text{P}_{1/2})$, then the internal energy of the $\text{CH}_2\text{CH}_2\text{ONO}$ radicals would shift 10.5 kcal/mol lower. Because angular momentum is conserved along each reaction pathway, some of the radicals with a total internal energy above the dissociation barrier may still be stable to subsequent dissociation due the large energy constrained to remain in rotational energy.

3.4. Branching Ratio between O–NO Bond Fission and C–Br Photofission. The data presented herein also allow us to determine the branching ratio between O–NO bond photofission and C–Br photofission.

$$\begin{aligned} \Phi_{\text{Br}} &= \left(\frac{\text{integrated counts at NO}^+}{\text{integrated counts at } ^{79}\text{Br}^+} \right) \left(\frac{50.69}{100} \right) \left(\frac{\sigma_{\text{Br}/\text{Br}^+}}{\sigma_{\text{NO}/\text{NO}^+}} \right) \left(\frac{\text{correction for Br}}{\text{correction for NO}} \right) \\ &= \left(\frac{7034}{3871} \right) \left(\frac{50.69}{100} \right) \left(\frac{3.14}{2.64} \right) \left(\frac{8909}{3192} \right) = 3.9 \end{aligned}$$

We begin by integrating both areas under the fits from 0 to 550 μs at $m/e = 30$ from NO atoms shown as the solid blue line (Figure 1) and $m/e = 79$ from ^{79}Br shown as the solid orange line (Figure 8), normalizing each to 1000 laser shots. Because we photodissociate molecules with both isotopes of Br but only integrate the signal in the ^{79}Br spectrum, we correct for the isotopic abundance of ^{79}Br , which is 0.5069. In addition, we must correct the integrated signal at each ion by the partial photoionization cross section of Br to form Br^+ , $\sigma_{\text{Br}/\text{Br}^+}$,²⁰ and NO to form NO^+ , $\sigma_{\text{NO}/\text{NO}^+}$.²¹ Finally, we must also include the usual correction due to the appropriate Jacobian factor, the three-dimensional scattering kinematics in the photodissociation, and the differing transit times through the ionization

region due to the neutral fragment velocities. To obtain that ratio, we calculate a hypothetical TOF spectrum by superimposing the signal from NO (from O–NO photofission) and Br (from C–Br photofission) in the same spectrum, assuming each has equal partial ionization cross sections, so each has a time-of-flight distribution consistent with the $P(E_T)$'s shown for NO in Figure 2 and for Br in Figure 9. We use this calculation to predict the relative integrated signal from NO and from Br over the same time range (0–550 μ s) that would be observed in the TOF spectra if they are produced in a 1:1 ratio, rather than scaling the fits to match the measured spectra. The high kinetic energy NO product is, as expected, discriminated against, so the actual integrated counts at NO^+ is divided by 3192, whereas the actual signal at Br^+ is divided by 8909. Although the partial ionization cross sections used here are accurate to 14%, the two respective contributions from Br and NO to the $m/e = 79$ TOF spectra and $m/e = 30$ TOF spectra overlap other signals in the spectra, so the uncertainty in this branching ratio is greater than 14%.

4. DISCUSSION

In this report, we focused on characterizing two of the primary photodissociation channels of $\text{BrCH}_2\text{CH}_2\text{ONO}$ at 193 nm and the subsequent unimolecular dissociation channels of the nascent $\text{BrCH}_2\text{CH}_2\text{O}$ radicals produced from the O–NO bond photofission. We also performed theoretical predictions on the possible subsequent unimolecular dissociation channels of the vibrationally excited $\text{CH}_2\text{CH}_2\text{ONO}$ radicals resulting from primary C–Br bond photofission. This work follows two studies of $\text{BrCH}_2\text{CH}_2\text{ONO}$ photodissociation at 351/355 nm by Wang et al.¹⁷ and Chhantyal-Pun et al.²² The only primary photodissociation channel of $\text{BrCH}_2\text{CH}_2\text{ONO}$ detected upon photodissociation at 351 nm was O–NO bond fission. C–Br photofission and HBr photoelimination do not compete significantly with O–NO photofission at this excitation wavelength. Even though the presence of the Br substituent does not alter the primary photodissociation channels at 351/355 nm, one might expect C–Br photofission to compete with O–NO photofission at 193 nm, as alkyl bromides have an excited state that is repulsive in the C–Br bond at those higher energies.

In this study, our data taken at 193 nm show that both O–NO photofission and C–Br photofission are major primary photodissociation channels; HBr photoelimination is definitely not a significant primary photodissociation channel. The branching ratio between the O–NO photofission channel and the C–Br photofission channel is 3.9, indicating that O–NO bond photofission is still the dominant primary photodissociation channel. The O–NO photofission channel is similar to that in the known photochemistry of alkyl nitrites in the absorption band accessed at 193 nm. The primary O–NO photodissociation $P(E_T)$ at 193 nm peaks near 30 kcal/mol, as compared to 14 kcal/mol at 351 nm. This is partly due to the higher available energy at 193 nm: 112 kcal/mol at 193 nm as compared to 45 kcal/mol at 351 nm. The competing C–Br fission channel is facilitated by the bichromophoric nature of the excited state of $\text{BrCH}_2\text{CH}_2\text{ONO}$ accessed at 193 nm. It is interesting to note that the absorption cross section of methyl nitrite and ethyl nitrite (CH_3ONO and $\text{CH}_3\text{CH}_2\text{ONO}$) is near 2.2 Mb,²³ whereas the absorption cross-section is near ~ 0.6 Mb at 193 nm for CH_3Br ²⁴ and ~ 0.7 Mb for $\text{CH}_3\text{CH}_2\text{Br}$.²⁵ The absorption cross sections are substantial in the single chromophore systems and these excited states are strongly

repulsive along the O–NO dissociation coordinate and the C–Br fission coordinate, respectively. Thus, one might expect the bichromophore $\text{BrCH}_2\text{CH}_2\text{ONO}$ to have an excited state of mixed character (a linear combination of two diabats, one from each excited electronic configuration) that would then result in a competition between C–Br and O–NO photofission.

The O–NO photofission channel at 193 nm produces $\text{BrCH}_2\text{CH}_2\text{O}$ radicals. Our measured kinetic energy distribution allows us to estimate the internal energy distribution in the nascent $\text{BrCH}_2\text{CH}_2\text{O}$ radicals (section 3.2.2). Due to the extra internal energy available for nascent $\text{BrCH}_2\text{CH}_2\text{O}$ radicals at 193 nm than 351 nm, no stable $\text{BrCH}_2\text{CH}_2\text{O}$ radicals are expected. Most of the radicals undergo subsequent dissociation to $\text{CH}_2\text{Br} + \text{H}_2\text{CO}$, in agreement with the theoretical prediction on the ground electronic state of $\text{BrCH}_2\text{CH}_2\text{O}$ and in accordance with our previous study at 351 nm. The translational energy distribution imparted during the secondary dissociation to $\text{CH}_2\text{Br} + \text{H}_2\text{CO}$ is broader and peaks near 12 kcal/mol at 193 nm as compared to 5 kcal/mol at 351 nm. Radicals generated at both wavelengths may experience repulsive forces after the transition state at 16 kcal/mol in Figure 3, but the secondary $P(E_{T,2^\circ})$ in Figure 4 evidence substantially more energy in translation than expected from a 7 kcal/mol exit barrier. This is likely due to the higher rotational energy of the $\text{BrCH}_2\text{CH}_2\text{O}$ produced at 193 nm; the tangential velocity at the higher rotational energy can shift the $P(E_{T,2^\circ})$ to larger energies. Some of the $\text{BrCH}_2\text{CH}_2\text{O}$ radicals dissociate to $\text{H} + \text{BrCH}_2\text{CHO}$. Because the loss of an H atom does not change the velocity of the heavy BrCH_2CHO cofragment, we see three signals at $m/e = 30, 79,$ and 29 that are momentum-matched to the NO cophotofragments. These signals cannot be from stable $\text{BrCH}_2\text{CH}_2\text{O}$ radicals; they result rather from dissociative ionization of BrCH_2CHO from the $\text{H} + \text{BrCH}_2\text{CHO}$ secondary channel.

In our previous study at 351 nm, we mentioned that Chhantyal-Pun et al.²² report strong spectroscopic evidence for a vinoxy radical product from the photodissociation of halogenated alkyl nitrites, including $\text{BrCH}_2\text{CH}_2\text{ONO}$. They attribute that signal to a competing channel in the dissociation of the nascent $\text{BrCH}_2\text{CH}_2\text{O}$ radicals, a channel that forms vinoxy + HBr. Our previous study at 351 nm¹⁷ showed that vinoxy cannot be from this source because the signal at HBr^+ is far too small to form in a 1:1 (or larger) ratio with vinoxy. In this study, we confirm this assumption again that there is insufficient HBr^+ signal from HBr to assign the vinoxy signal to the $\text{BrCH}_2\text{CH}_2\text{O} \rightarrow \text{vinoxy} + \text{HBr}$ reaction.

In this study, we also estimated the vibrational energy distributions of the nascent *trans*- $\text{CH}_2\text{CH}_2\text{ONO}$ radicals formed from the four conformers of the precursor. Some of the radicals may be stable to subsequent dissociation due to the large proportion of rotational energy. We have just begun a study of the secondary dissociation channels of $\text{CH}_2\text{CH}_2\text{ONO}$ after C–Br bond fission at 193 nm, in which we investigate several sources of the signal at $m/e = 42$ detected with electron bombardment ionization and the tiny vinoxy signal at $m/e = 43$ detected with photoionization.

■ ASSOCIATED CONTENT

● Supporting Information

The Supporting Information includes the optimized geometries of the four conformers of $\text{BrCH}_2\text{CH}_2\text{ONO}$ used to estimate the angular momentum of the $\text{CH}_2\text{CH}_2\text{ONO}$ radicals resulting from C–Br photofission, and the J distributions of the *trans*-

CH₂CH₂ONO radicals from each conformer as a function of total internal energy in the radical. The Supporting Information is available free of charge on the ACS Publications website at DOI: 10.1021/acs.jpca.5b04162.

AUTHOR INFORMATION

Corresponding Author

*E-mail: L-Butler@uchicago.edu.

Notes

The authors declare no competing financial interest.

ACKNOWLEDGMENTS

This work was supported by the Chemical Sciences, Geosciences and Biosciences Division, Office of Basic Energy Sciences, Office of Science, U.S. Department of Energy, under Grant DE-FG02-92ER14305 (L.J.B.). T.D.R. was supported by the Arnold and Mabel Beckman Foundation as a Beckman Scholar.

REFERENCES

- (1) Wayne, R. P. *Chemistry of Atmospheres*, 3rd ed.; Oxford University: Oxford, U.K., 2000.
- (2) Dixon, R. N.; Rieley, H. State-selected Photodissociation Dynamics of HONO (\tilde{A}^1A''): Characterization of the NO Fragment. *J. Chem. Phys.* **1989**, *91*, 2308–2320.
- (3) Vasudev, R.; Zare, R. N.; Dixon, R. N. Dynamics of Photodissociation of HONO at 369 nm: Motional Anisotropy and Internal State Distribution of the OH Fragment. *Chem. Phys. Lett.* **1983**, *96*, 399–402.
- (4) Vasudev, R.; Zare, R. N.; Dixon, R. N. State-Selected Photodissociation Dynamics: Complete Characterization of the OH Fragment Ejected by the HONO \tilde{A} State. *J. Chem. Phys.* **1984**, *80*, 4863–4878.
- (5) Brühlmann, U.; Dubs, M.; Huber, J. R. Photodissociation of Methylnitrite: State Distributions, Recoil Velocity Distribution, and Alignment Effects of the NO($X^2\Pi$) Photofragment. *J. Chem. Phys.* **1987**, *86*, 1249–1257.
- (6) Benoist d'Azy, O.; Lahmani, F.; Lardeux, C.; Solgadi, D. State-Selective Photochemistry: Energy Distribution in the NO Fragment after Photodissociation of the CH₃ONO $n\pi^*$ State. *Chem. Phys.* **1985**, *94*, 247–256.
- (7) Lahmani, F.; Lardeux, C.; Solgadi, D. Rotational and Electronic Anisotropy in NO $X^2\Pi$ from the Photodissociation of CH₃ONO. *Chem. Phys. Lett.* **1986**, *129*, 24–30.
- (8) Schwartz-Lavi, D.; Bar, I.; Rosenwaks, S. Rotational Alignment and Non-Statistical Λ Doublet Population in NO Following (CH₃)₃CONO Photodissociation. *Chem. Phys. Lett.* **1986**, *128*, 123–126.
- (9) Winniczek, J. W.; Dubs, R. L.; Appling, J. R.; McKoy, V.; White, M. G. A Multiphoton Ionization Study of the Photodissociation Dynamics of the S₂ State of CH₃ONO. *J. Chem. Phys.* **1989**, *90*, 949–963.
- (10) Yin, H. M.; Sun, J. L.; Li, Y. M.; Han, K. L.; He, G. Z. Photodissociation Dynamics of the S₂ State of CH₃ONO: State Distributions and Alignment Effects of the NO ($X^2\Pi$) Photofragment. *J. Chem. Phys.* **2003**, *118*, 8248–8255.
- (11) Finke, H.; Spiecker, H.; Andresen, P. The Photodissociation of tert-Butyl Nitrite at 193 nm. *J. Chem. Phys.* **1999**, *110*, 4777–4782.
- (12) Schwartz-Lavi, D.; Rosenwaks, S. Scalar and Vectorial Properties in the Photodissociation of tert-Butyl Nitrite from the S₁ and S₂ States. *J. Chem. Phys.* **1988**, *88*, 6922–6930.
- (13) Hippler, M.; Al-Janabi, F. A. H.; Pfab, J. Photodissociation of Jet-Cooled Methyl and t-Butyl Nitrite near 380 nm. *Chem. Phys. Lett.* **1992**, *192*, 173–178.
- (14) Castle, K. J.; Abbott, J.; Peng, X.; Kong, W. Photodissociation of t-Butyl Nitrite Between 200 and 250 nm: Internal Energy Distribution of NO. *Chem. Phys. Lett.* **2000**, *318*, 565–570.
- (15) Farmanara, P.; Stert, V.; Radloff, W. Ultrafast Photodissociation of Methyl Nitrite Excited to the S₂ State. *Chem. Phys. Lett.* **1999**, *303*, 521–525.
- (16) Mestdagh, J. M.; Berdahl, M.; Dimicoli, I.; Mons, M.; Meynadier, P.; d'Oliveira, P.; Piuze, F.; Visticot, J. P.; Jouvet, C.; Lardeux-Dedonder, C.; Martrenchard-Barra, S.; Soep, B.; Solgadi, D. Observation of an Indirect Pathway in the Femtosecond Study of Alkyl Nitrite Photodissociation in the S₁ State. *J. Chem. Phys.* **1995**, *103*, 1013.
- (17) Wang, L.; Lam, C.-S.; Chhantyal-Pun, R.; Brynteson, M. D.; Butler, L. J.; Miller, T. A. Imaging and Scattering Studies of the Unimolecular Dissociation of the BrCH₂CH₂O Radical from BrCH₂CH₂ONO Photolysis at 351 nm. *J. Phys. Chem. A* **2014**, *118*, 404–416.
- (18) Keller, B. A.; Felder, P.; Huber, J. R. Molecular Beam Photodissociation Study of Methyl Nitrite In the Near-Ultraviolet Region. *J. Phys. Chem.* **1987**, *91*, 1114–1120.
- (19) McKown, B. G.; Ceriotti, M.; Womack, C. C.; Kamarchik, E.; Butler, L. J.; Bowman, J. M. Effects of High Angular Momentum on the Unimolecular Dissociation of CD₂CD₂OH: Theory and Comparisons with Experiment. *J. Phys. Chem. A* **2013**, *117*, 10951–10963.
- (20) Hayes, T. R.; Wetzel, R. C.; Freund, R. S. Absolute Electron-impact-ionization Cross-section Measurements of the Halogen Atoms. *Phys. Rev. A: At, Mol., Opt. Phys.* **1987**, *35*, 578–584.
- (21) Iga, I.; Rao, M. V. V. S.; Srivastava, S. K. Absolute Electron Impact Ionization Cross Sections for N₂O and NO from Threshold up to 1000 eV. *J. Geophys. Res.* **1996**, *101*, 9261–9266.
- (22) Chhantyal-Pun, R. C.; M, -W.; Sun, D.; Miller, T. A. Detection and Characterization of Products from Photodissociation of XCH₂CH₂ONO (X = F, Cl, Br, OH). *J. Phys. Chem. A* **2012**, *116*, 12032–12040.
- (23) Maricq, M. M.; Wallington, T. J. Absolute Ultraviolet Cross Sections of Methyl and Ethyl Peroxy Radicals. *J. Phys. Chem.* **1992**, *96*, 986–992.
- (24) Robbins, D. E. UV Photoabsorption Cross Sections for Halocarbons. *International Conference on Problems Related to the Stratosphere: held at Utah State University, Logan, Utah, September 15-17, 1976*; JPL: Pasadena, CA, 1976; No. 77-12; pp 255–257.
- (25) Giuliani, A.; Motte-Tollet, F.; Delwiche, J.; Mason, N. J.; Jones, N. C.; Gingell, J. M.; Walker, I. C.; Hubin-Franskin, M.-J. Electronic Excitation and Oscillator Strength of Ethyl Bromide by Vacuum Ultraviolet Photoabsorption and Electron Energy Loss Spectroscopy. *J. Chem. Phys.* **2000**, *112*, 6285–6292.

NOTE ADDED AFTER ASAP PUBLICATION

This article was published ASAP on July 13, 2015, with an incorrect version of Figure 10. The corrected article was published ASAP on July 23, 2015.